



An improved constrained simultaneous iterative reconstruction technique for ionospheric tomography

Yibin Yao¹ · Changzhi Zhai¹ · Jian Kong² · Cunjie Zhao¹ · Yiyong Luo¹ · Lei Liu¹

Received: 28 May 2019 / Accepted: 6 April 2020 / Published online: 18 April 2020
© Springer-Verlag GmbH Germany, part of Springer Nature 2020

Abstract

Global Navigation Satellite System (GNSS) is now widely used for continuous ionospheric observations. Three-dimensional computerized ionospheric tomography (3DCIT) is an important tool for the reconstruction of electron density distributions in the ionosphere through effective use of the GNSS data. More specifically, the 3DCIT technique is able to resolve the three-dimensional electron density distributions over the reconstructed area based on the GNSS slant total electron content (STEC) observations. We present an Improved Constrained Simultaneous Iterative Reconstruction Technique (ICSIRT) algorithm that differs from the traditional ionospheric tomography methods in 3 ways. First, the ICSIRT computes the electron density corrections based on the product of the intercept and electron density within voxels so that the assignment of corrections at different heights becomes more reasonable. Second, an Inverse Distance Weighted (IDW) interpolation is used to restrict the electron density values in the voxels not traversed by GNSS rays, thereby ensuring the smoothness of the reconstructed region. Also, to improve the reconstruction accuracy around the HmF2 (the peak height of the F2 layer) altitude, a multiresolution grid is adopted in the vertical direction, with a 10-km resolution from 200 to 420 km and a 50-km resolution at other altitudes. The new algorithm has been applied to the GNSS data over the European and North American regions in different case studies that involve different seasonal conditions as well as a major storm. In the European region experiment, reconstruction results show that the new ICSIRT algorithm can effectively improve the reconstruction of the GNSS data. The electron density profiles retrieved from ICSIRT are much closer to the ionosonde observations than those from its predecessor, namely, the Constrained Simultaneous Iteration Reconstruction Technique (CSIRT). The reconstruction accuracy is significantly improved. In the North American region experiment, the electron density profiles in ICSIRT results show better agreement with incoherent scatter radar observations than CSIRT, even for the topside profiles.

Keywords Three-dimensional computerized ionospheric tomography · Electron density · GNSS · Simultaneous iteration reconstruction technique

Introduction

Changes of ionospheric electron density are very complicated since the ionosphere is controlled by many factors, such as solar radiation, geomagnetic storms triggered by coronal mass ejections, magnetic field variations, and

neutral atmosphere fluctuations. Various parameters are used to monitor and describe the ionosphere, including electron and ion temperature, electron and ion density, and the critical frequency of the F2 density peak. Electron density is the most important ionospheric parameter. Changes in electron density in the ionosphere not only reflect the coupling process of the magnetosphere–ionosphere–thermosphere system but also have a significant influence on radio communication and satellite navigation. Therefore, an accurate reconstruction of the electron density distribution in the ionosphere is very important for ionospheric research.

Three-dimensional computerized ionospheric tomography (3DCIT) based on the GNSS data has been frequently applied in ionospheric reconstruction because of its advantages of low cost as well as fast and wide monitoring range.

✉ Changzhi Zhai
czzhai@whu.edu.cn

✉ Jian Kong
jkong@whu.edu.cn

¹ School of Geodesy and Geomatics, Wuhan University, Wuhan 430079, China

² Chinese Antarctic Center of Surveying and Mapping, Wuhan University, Wuhan 430079, China

Austen et al. (1988) first proposed the concept of ionospheric tomography and carried out a computer simulation experiment. A large number of theoretical (Markkanen et al. 1995; Kunitsyn et al. 1997; Raymond et al. 1994) and experimental studies (Kersley et al. 1993; Huang et al. 1999; Pryse et al. 1997) have been carried out using two-dimensional ionospheric tomography based on low orbit satellites. Ionospheric tomography is typically an ill-posed problem due to the sparsity of the GNSS stations and the limitation of elevation angles of available rays. To solve this problem, Andreeva et al. (1990) and Kunitsyn et al. (1994a, b, 1995) applied the Algebraic Reconstruction Technique (ART) algorithm proposed by Gordon et al. (1970) in ionospheric tomography experiments. Several new methods are also based on ART algorithms such as Hybrid Reconstruction Algorithm (HRA) (Wen et al. 2008) and Improved Algebraic Reconstruction Technique (IART) (Wen et al. 2007). The Multiplicative Algebraic Reconstruction Technique (MART) was presented by Gordon et al. (1970) for the first time and used in CIT (computerized ionospheric tomography) by Raymond et al. (1990). This algorithm is based on maximum entropy estimation, which can make the inversion result consistent with the observed data and avoids negative values in the inversion result. A two-step algorithm was presented by Wen et al. (2012) in which Phillips smoothing method (PSM) was first used to resolve the ill-posed problem in 3DCIT and then used as an initial value to the MART method. Yao et al. (2014) investigated a 3-D iterative reconstruction algorithm based on the minimization of total variations and conducted numerical experiments under quiet condition and also geomagnetic storms. Norberg et al. (2015) used Bayesian statistical inversion to stabilize the ill-posed problem in 3DCIT and used a Gaussian Markov random field priors to overcome the computational difficulties with full covariance matrices. Kong et al. (2016) split the ionosphere into four layers and employed the Kalman filtering method to estimate the parameters. Side rays are employed in 3DCIT, and the partial slant total electron content (STEC) of side rays is obtained based on NeQuick2 model and GNSS (Yao et al. 2018).

The simultaneous Iteration Reconstruction Technique (SIRT) is a development of the ART algorithm. SIRT makes corrections for voxels after all the ray paths have been considered, instead of one ray path at a time, to avoid the overcorrection of voxels that are traversed by multiple GNSS rays (Pryse et al. 1993; Bust and Mitchell 2008). At present, the reconstruction algorithms mainly use observational data to improve the background so that it approximates the actual ionosphere state. All the algorithms mentioned above use the GNSS rays to improve the voxels, but voxels that are not crossed by rays cannot be corrected. Wen et al. (2010) proposed a Constrained Algebraic Reconstruction Technique (CART) which uses the

second-order Laplace operator to provide the constraint matrix. An Adaptive Simultaneous Algebraic Reconstruction Technique (ASART) is presented by Wan et al. (2011) in which an adaptive relaxation parameter and a modified multilevel access scheme are developed to improve the accuracy of the reconstructed 3D structure. The Gauss weighting function is introduced to constrain the tomography system by Debaio et al. (2015) in Constrained Adaptive Simultaneous Algebraic Reconstruction Technique (CASART). The numerical simulation and actual GPS data experiment results show that the Gauss weighting function can resolve the problem of initial values dependence and improve the electron density reconstruction. Liu et al. (2010) proposed the Constrained Simultaneous Iteration Reconstruction Technique (CSIRT) algorithm in which the Laplacian operator is used to smooth the voxels of the entire inversion region. In the smoothing process, the voxels not traversed by the GNSS rays would be improved by the surrounding traversed voxels and the whole inversion region is ultimately improved.

In the smoothing process using the Laplacian operator, if a voxel is crossed and corrected by the GNSS rays and the surrounding voxels are not, the correction will be partially or entirely offset due to smoothing. This eventually leads to incomplete correction of the inversion area, and the observational data are not adequately utilized. In addition, electron density corrections are assigned to voxels according to the intercepts of the ray paths within them, while the corrections are also proportional to electron densities at the voxels. Therefore, it is unreasonable to allocate the corrections according to the intercept only. This causes overcorrection at the bottom and top regions, which have small electron densities, and causes insufficient correction at the middle region, which has large electron densities. To solve these problems, we present an ICSIRT algorithm. In the ray correction process, the electron density of the voxels is introduced into the correction assignment, which makes the correction distribution a better fit with the electron density distribution along its height. The IDW interpolation is applied to correct the voxels not traversed by the GNSS rays. To evaluate the feasibility and superiority of the new algorithm, we conducted a set of experiments using the GNSS data over the European region and the North American region. The reconstruction residual is calculated, and electron density profiles are compared with ionosonde and ISR observations.

Reconstruction technique

The slant total electron content (STEC) is estimated from carrier phase smoothed pseudorange,

$$STEC = \frac{f_1^2 f_2^2}{40.3(f_1^2 - f_2^2)} (\tilde{p}_2 - \tilde{p}_1 + \Delta b_k + \Delta b^s) \tag{1}$$

where f_1 and f_2 are the frequencies of the GNSS signals, \tilde{p}_1 and \tilde{p}_2 are the carrier phase smoothed pseudoranges, Δb_k indicates the differential code bias (DCB) of the receivers, and Δb^s represents the differential code bias of the satellites. The DCBs of the satellites and receivers are corrected before the STEC measurements are used in the inversion. The details of the DCB estimation can be found in Jin et al. (2012).

STEC along the GNSS ray path can be represented as:

$$STEC = \int_l Ne(\vec{r}, t) ds \tag{2}$$

where Ne is the electron density of position \vec{r} and time t , and l is the signal propagation path. The inversion region can be divided into small voxels, and the STEC measurements can be formulated as:

$$STEC_{m \times 1} = A_{m \times n} \cdot x_{n \times 1} + \epsilon_{m \times 1} \tag{3}$$

where m is the number of TEC measurements, n is the number of the voxels in the inversion region, A is the design matrix, x is the vector consisting of all the unknown electron densities in all voxels, and ϵ is an error column vector of TEC measurement noises.

For $k + 1$ th iteration, the j th voxel is calculated in the SIRT algorithm as follows:

$$x_j^{k+1} = x_j^k + \frac{1}{P} \sum_{i=1}^P \lambda \cdot \Delta \cdot W$$

$$\Delta = y_i - \sum_{m=1}^M A_{i,m} x_m^k \tag{4}$$

$$W = \frac{A_{i,j}}{\sum_{m=1}^M A_{i,m}^2}$$

where x_j^{k+1} is the ray-corrected electron density value of the j th voxel after $k + 1$ iterations, P is the number of voxels traversed by the i th ray with $0 \leq P \leq n$, and λ is the relaxation parameter $0 \leq \lambda \leq 1$, and is set to 0.2 in this study. y_i is the GNSS TEC of the i th ray, $A_{i,m}$ is the intercept of the i th ray in the m th voxel, Δ is the correction of the i th ray path, and W is the weight of the j th voxel for the i th ray TEC correction assignment. The iteration will stop when the maximum value of the difference between current iteration and last iteration result is smaller than $0.03 \times 10^{11} \text{ e/m}^3$ or the number of iterations is more than 20.

Correction assignment method considering electron density

It is known from (4) that the ray correcting process can be divided into two processes, e.g., correction calculation and correction assignment. In the correction calculation process, $\sum_{m=1}^M A_{i,m} x_m^k$ is the integral of the intercept and electron density within the voxels along the i th ray path. That means that the correction is inversely proportional to the product of the electron density and intercept. However, in the correction assignment process of reconstruction algorithms such as ART, MART and CSIRT, the correction is assigned to voxels only according to intercept.

The ray path correction assignment diagram of a latitudinal plane is given in Fig. 1. If $A_{i,j} = A_{i,k}$, then the corrections of the j th voxel and k th voxel are the same. Actually, the corrections should be different since the electron densities and their variation of voxels j and k vary greatly. Therefore, the correction assignment process is not reasonable. We proposed a correction assignment method that distributes the correction by the product of intercept and electron density:

$$W = \frac{A_{i,j} \cdot x_j^k}{\sum_{m=1}^M A_{i,m} \cdot x_m^k} \cdot \frac{1}{A_{i,j}}$$

$$= \frac{x_j^k}{\sum_{m=1}^M A_{i,m} \cdot x_m^k} \tag{5}$$

where $\frac{1}{A_{i,j}}$ is used to convert the TEC correction to the electron density correction. Please note that the denominator of W is also changed from $\sum_{m=1}^M A_{i,m}^2$ to $\sum_{m=1}^M A_{i,m} \cdot x_m^k$. Thus, the correction assignment is changed from intercept square to the product of intercept and electron density.

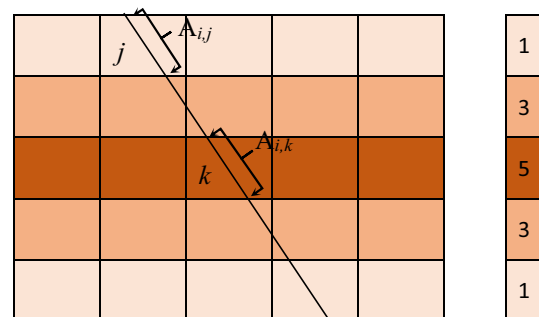


Fig. 1 Ray path correction assignment diagram of a latitudinal plane. The black line is the GNSS ray path, $A_{i,j}$ and $A_{i,k}$ represents the intercept of the i th ray path in the j th and k th voxels, respectively. The color bar on the right symbolically gives the electron density value of different heights

Inverse distance weighted interpolation

As mentioned above, the earth’s ionosphere is a partially ionized gas that is influenced by many factors, both from the sun and from the neutral atmosphere. In previous studies, the Laplacian operator is applied to smooth the inversion region after one iteration in the ray correcting process of CSIRT(Wen et al. 2010; Liu et al. 2010; Hobiger et al. 2008).

Figure 2 shows the diagram of 2D voxels. For the center voxel, the Laplacian operator can be expressed as

$$L_0 = \begin{vmatrix} -1 & -1 & -1 \\ -1 & 8 & -1 \\ -1 & -1 & -1 \end{vmatrix} \tag{6}$$

the operator has to be adjusted for the voxels at the corners:

$$\begin{aligned} L_1 &= \begin{vmatrix} -1 & -1 \\ 3 & -1 \end{vmatrix} & L_2 &= \begin{vmatrix} -1 & -1 \\ -1 & 3 \end{vmatrix} \\ L_3 &= \begin{vmatrix} 3 & -1 \\ -1 & -1 \end{vmatrix} & L_4 &= \begin{vmatrix} -1 & 3 \\ -1 & -1 \end{vmatrix} \end{aligned} \tag{7}$$

and the operator is expressed as follows for voxels on the edge:

$$\begin{aligned} L_5 &= \begin{vmatrix} -1 & -1 & -1 \\ -1 & 5 & -1 \end{vmatrix} & L_6 &= \begin{vmatrix} -1 & 5 & -1 \\ -1 & -1 & -1 \end{vmatrix} \\ L_7 &= \begin{vmatrix} -1 & -1 & -1 \\ -1 & 5 & -1 \end{vmatrix}^T & L_8 &= \begin{vmatrix} -1 & 5 & -1 \\ -1 & -1 & -1 \end{vmatrix}^T \end{aligned} \tag{8}$$

The voxels traversed by the rays would be corrected after each iteration while the voxels without traversed rays will be

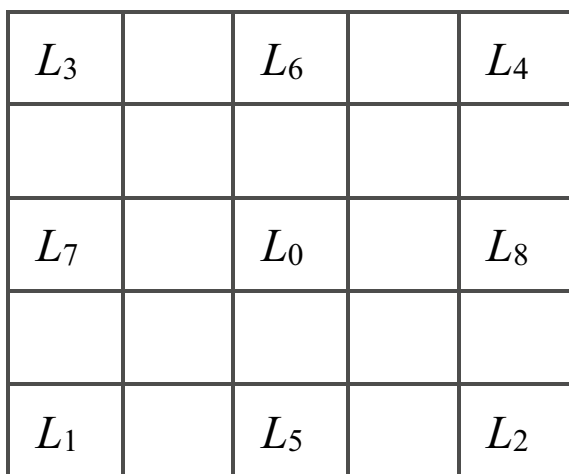


Fig. 2 Diagram of the 2D inversion region

corrected after smoothing if they are surrounded by voxels traversed by the rays. However, if one voxel, e.g., L_0 , is corrected by the rays and the voxels around it are not corrected, the ray correction of L_0 will be offset by the smoothing process. This will cause excessive smoothing. To cope with the problem, we applied the Inverse Distance Weighted (IDW) interpolation to correct the voxels that are not traversed by the rays. Like the Laplacian operator method, the correction value of the center cell is also transferred from neighboring cells. However, the IDW assumes that the values of the cells that are close to the center cell are more alike than those that are further apart(Ge et al. 2003). The IDW interpolation has been used in regional ionospheric delay interpolation in satellite-based augmentation systems (SBAS) such as GPS Aided Geo Augmented Navigation (GAGAN) system and GPS Wide-Area Augmentation System (WAAS) (El Arini et al. 1994; Ge et al. 2003; Prasad and Sarma 2007). A general form of IDW is defined as follows:

$$x_0 = \frac{\sum_{i=1}^S \frac{x_i}{d_i}}{\sum_{i=1}^S \frac{1}{d_i}} \tag{9}$$

where x_0 is the electron density value of interpolated voxel, x_i is the electron density value corrected by rays, d_i is the distance between interpolated voxel and rays corrected voxel, and S is the total number of rays corrected voxels. The electron density values of the ray corrected voxels will not be influenced by IDW since only voxels not traversed by the rays will be corrected.

Simulation experiment

The GNSS data from European Reference Frame Permanent Network (EUREF) on March 17, 2013, are used in the simulation experiment. The inversion region covered 40°–60° N in latitude and 0°–20° E in longitude, and the height ranged from 100 to 800 km. Since electron density exhibits largest altitude gradients around HmF2, a multi-vertical resolution is chosen in ICSIRT approach, with a 10-km resolution from 200 to 420 km and 50 km at other altitudes. The horizontal resolution is 1° in the latitude and longitude. The simulation region and GNSS station distribution are shown in Fig. 3. The time window for every inversion is 10 min, and there are about 2000 measurements from 35 GNSS stations used.

The positions of the GNSS rays are determined by GNSS stations and satellite orbits. The electron density values obtained from NeQuick2 on March 17, 2013, are used as Truth and June 20, 2013, is used as 3DCIT background. Simulated STEC values are integrated along the GNSS ray paths, and 10% random noise is added.

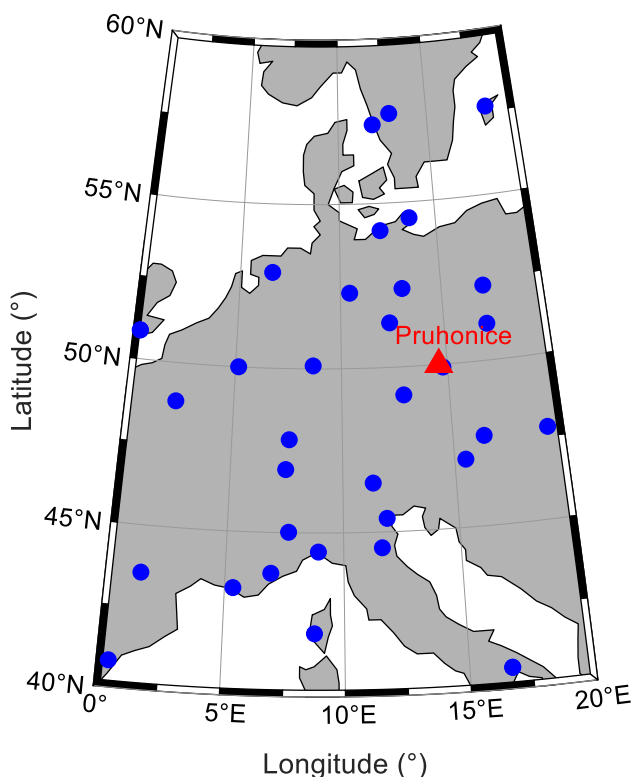


Fig. 3 European inversion area and distribution of GNSS stations and the Pruhonice ionosonde station. The blue dots represent the GNSS stations, and the red triangle represents the ionosonde station at Pruhonice

$STEC_i^{GNSS}$ is the GNSS STEC measurement of the i th ray and $STEC_i^{3DCIT}$ is the STEC value integrated from the 3DCIT results. The variation of the reconstruction residual in the reconstruction process reflects whether the reconstruction process converges and the degree of improvement of the reconstruction area. Figure 4 gives the simulation residuals comparison between CSIRT (blue) and ICSIRT (red) at 00 UT and 12 UT. As we can see, at 00 UT, the converged residual of CSIRT is about 2.3 TECU and ICSIRT is about 0.8 TECU. At 12 UT, the converged simulation residuals of CSIRT and ICSIRT are 7.0 TECU and 2.2 TECU, respectively. The converged simulation residuals are significantly lower than CSIRT.

Figure 5 shows a comparison between CSIRT and ICSIRT simulation results at 00:00 UT for 10°E height-latitude slices. The Background electron density values are much larger than the Truth. After reconstruction, the electron density is reduced in both of CSIRT and ICSIRT simulation results. But the ICSIRT simulation results are closer to the Truth than CSIRT as the maximum value of ICSIRT simulation results is about 3×10^{11} el/m³ and CSIRT is about 4×10^{11} el/m³.

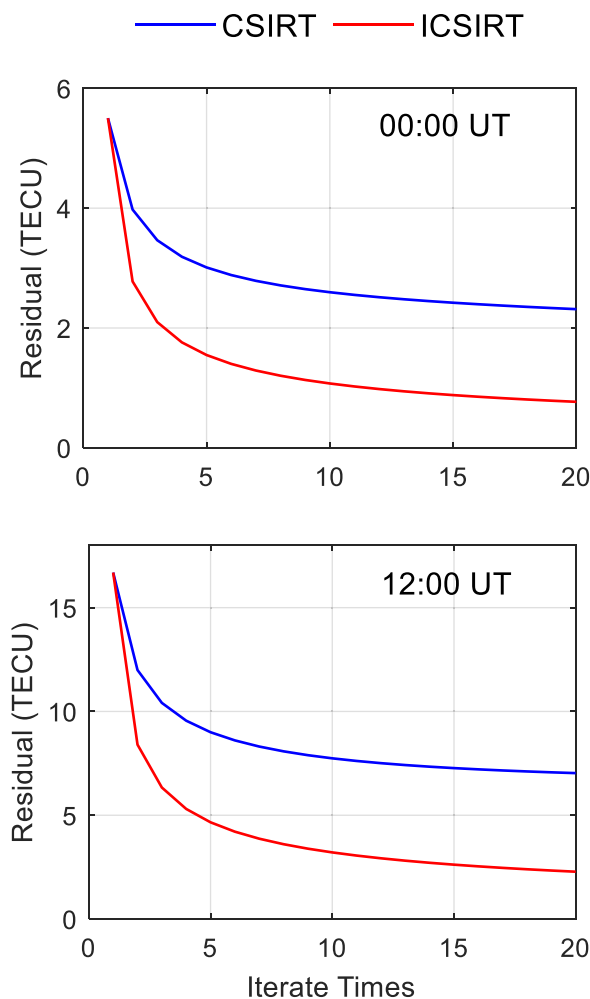


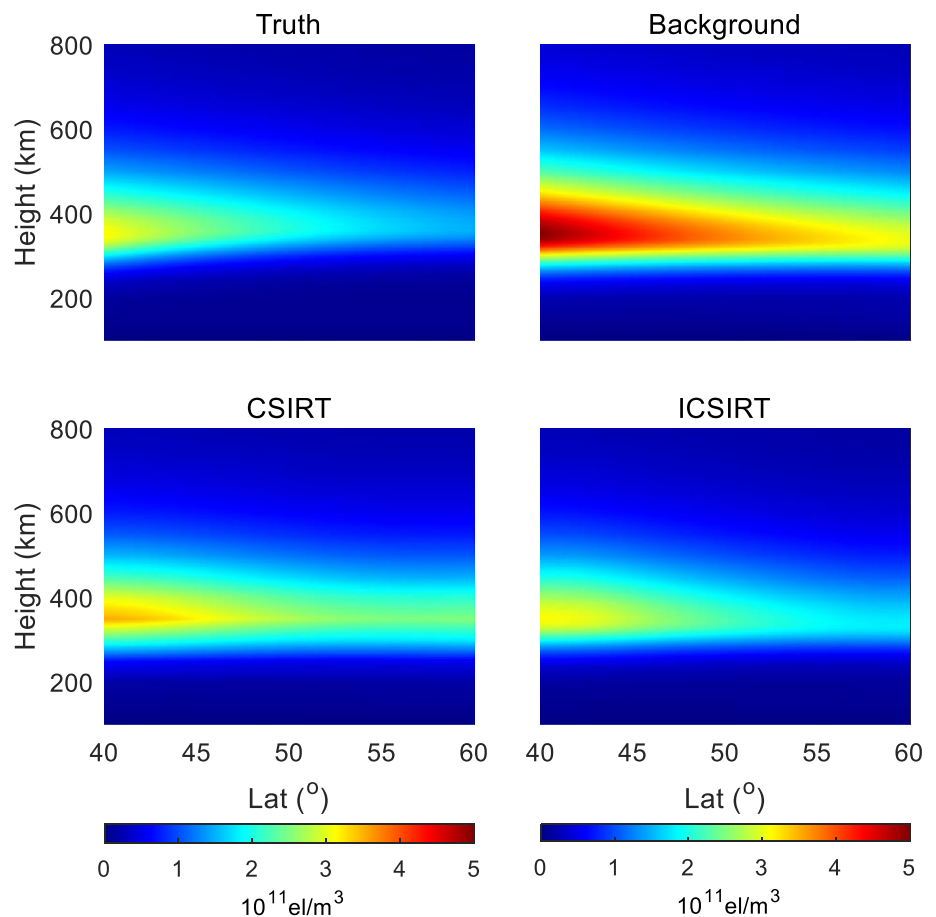
Fig. 4 Comparison of the simulation residuals of ICSIRT and CSIRT results. The blue and red curves correspond to the simulation residuals of CSIRT and ICSIRT, respectively

Figure 6 shows the comparison of simulation results at 12:00 UT. It can be seen that the Background electron density is enhanced by CSIRT and ICSIRT in simulation results, and the HmF2 is about 300 km, which is close to Truth. CSIRT and ICSIRT all show a little overestimation around 200 km, but the F2 peak height electron density of ICSIRT simulation results is larger and closer to Truth. Two periods of simulations show that the ICSIRT method is more effective than CSIRT.

Real data experiment: European region

A 3D ionospheric model is reconstructed based on the GNSS data from the European Reference Frame Permanent Network (EUREF) (Bruyninx et al. 2019), using CSIRT and ICSIRT and compared to the ionosonde data from Pruhonice station (Galkin et al. 2012; Reinisch and Galkin 2011). Five

Fig. 5 Truth, Background and simulation results of CSIRT and ICSIRT at 00:00 UT of March 17, 2013. The Truth and Background values are obtained from NeQuick2 at 00:00 UT on March 17, 2013, at and 00:00 UT on June 20, 2013, respectively



days in 2013 are selected that represent a quiet day before the geomagnetic storm (March 16), the major storm (March 17), summer solstice (June 20), equinox (September 22), and winter solstice (December 22) conditions, respectively. The inversion area and distribution of the GNSS stations are the same for the simulation experiment, and the Pruhonice ionosonde station is shown in Fig. 3. The electron density values obtained from NeQuick2 are used as background. Here we assume that the electron densities of the voxels are constant for ten minutes. To avoid unsmoothness in some extreme cases, we used the Laplacian operator in the last iteration in ICSIRT.

The interplanetary magnetic field (IMF), solar wind parameters and Dst index are shown in Fig. 7. The panels from top to bottom are IMF By component, Bz component, solar wind speed and Dst index. The shaded regions denote the day of March 17, 2013. The shock arrived at about 06:00 UT and IMF Bz turned southward. Solar wind speed was more than 700 km/s. Dst index was about -90 nT at 10:00 UT and then reached -130 nT at 20:00 UT.

Since the height of the inversion range is from 100 to 800 km and the GNSS satellites orbit altitude is about 20200 km, it is necessary to estimate the plasmaspheric

contribution to the GNSS STEC measurements. Shim et al. (2017) investigated the global morphology of the plasmaspheric TEC with the GPS TEC measurements board on Jason 1 and found that local time variations of plasmaspheric TEC is significantly smaller than ionospheric TEC. The IRI_Plas model (Gulyaeva 2002) is a combination of the IRI (version IRI-2001) model and the Standard Model of the Ionosphere and Plasmasphere (SMI) (Chasovitin 1998). The ionospheric empirical model NeQuick2 is a time-dependent three-dimensional ionospheric electron density model (Nava et al. 2008). Zhang et al. (2017) compared the topside ionospheric and plasmaspheric electron content (800 to 20,200 km) of the IRI_Plas model with COSMIC measurements, and their study showed that the IRI_Plas model is able to reproduce reasonably well the main features of the observed topside ionospheric and plasmaspheric latitudinal, diurnal, as well as seasonal variation tendency. Cherniak and Zakharenkova (2016) analyzed the performance of NeQuick2 and IRI_Plas model above 500 km with TerraSAR-X satellites and the two models showed similar precision. Thus, we employ the NeQuick2 model to calculate the partial STEC above the inversion top height and compare it with the total STEC along the GNSS rays.

Fig. 6 Truth, Background and simulation results of CSIRT and ICSIRT at 12:00 UT on March 17, 2013. The Truth and Background values are obtained from NeQuick2 at 12:00 UT on March 17, 2013, at and 12:00 UT on June 20, 2013, respectively

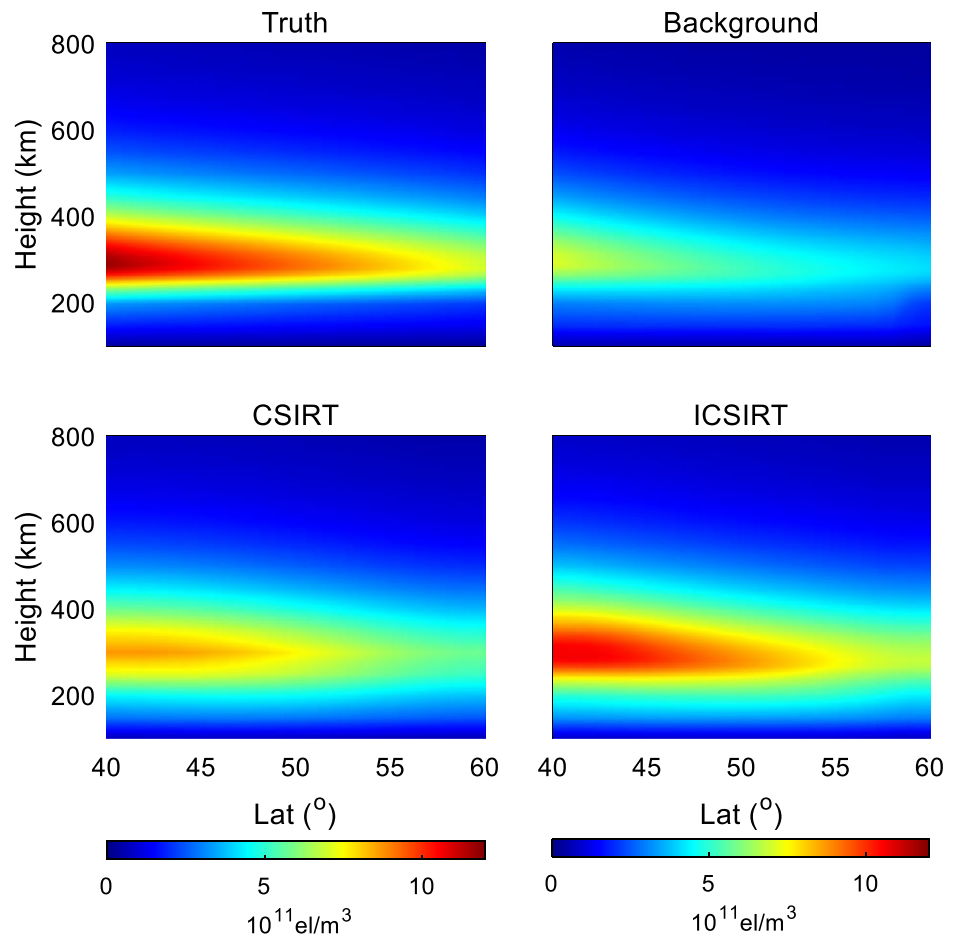
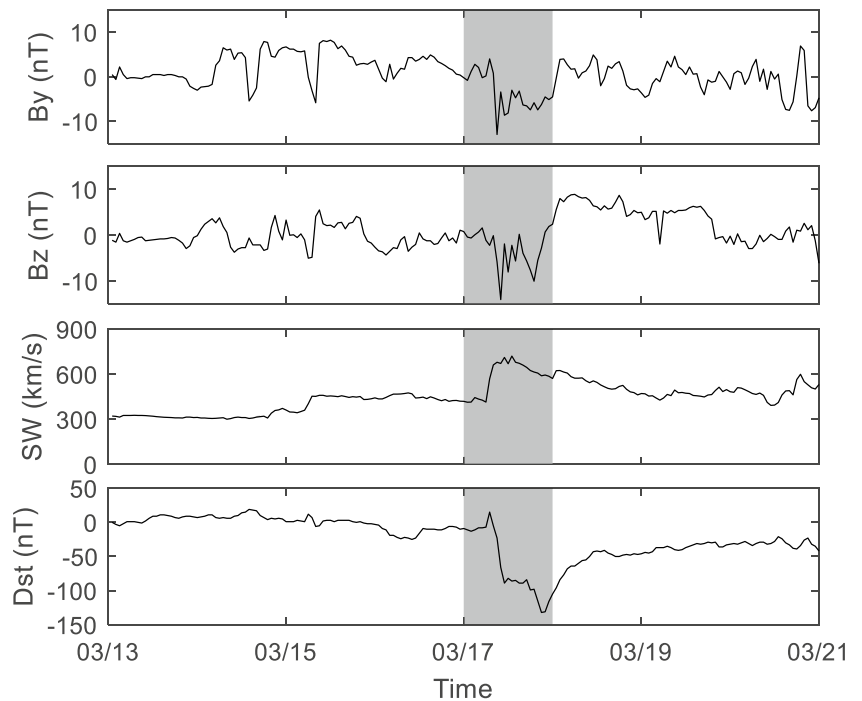


Fig. 7 Interplanetary magnetic field and solar wind parameters and Dst index around the March 17, 2013 geomagnetic storm



After the reconstruction of the inversion region, reconstruction STECs can be integrated based on the position of the GNSS rays and 3DCIT results. The reconstruction residual is calculated as follows:

$$\text{Residual} = \frac{\sum_{i=1}^n |\text{STEC}_i^{\text{GNSS}} - \text{STEC}_i^{\text{3DCIT}}|}{n} \quad (10)$$

Reconstruction residuals can show the algorithm efficiency and convergence condition through iterations.

Figure 8 shows the comparison of reconstruction residuals between ICSIRT and CSIRT results at 00 UT, 06 UT and 12 UT of March 17, 2013. As the residual values tend to stabilize after 10 iterates, the residual value at the 20th iteration is taken as the converged residual. As seen from Fig. 8, the converged residuals of CSIRT and ICSIRT at 00 UT are 2.1 TECU and 0.8 TECU, respectively. The converged residual of the ICSIRT algorithm is 61.9% lower than that of CSIRT. Similarly, at 06 UT and 12 UT, converged residuals of ICSIRT improved by 59.3% and 37.5%, respectively, compared to CSIRT. In addition, the residuals of the CSIRT at 00 UT and 06 UT show slight increases after reaching minima, and this is because the corrections are offset by Laplacian operator smoothing. The residuals of the ICSIRT show a steady decline or remain flat in all results. The comparison indicates that the ICSIRT algorithm yields a much improved ionosphere reconstruction compared to the CSIRT algorithm.

To compare the effects of the two algorithms to the background, NeQuick2 and the difference between the reconstruction results and background at 00 UT, 06 UT and 12 UT on March 16, March 17, June 20, September 22, December 22, 2013, are shown in Figs. 9, 10, 11, 12, 13, respectively. The first column is the NeQuick2 background ionosphere, the second column is the differences between the CSIRT results and the NeQuick2 background, and the third column is the differences between the ICSIRT results and the NeQuick2 background.

Figure 9 shows the NeQuick2 background and the difference between the reconstruction results and the background at 00 UT, 06 UT and 12 UT on March 16, 2013. The maximum difference between CSIRT and background at 00 UT is about $0.6 \times 10^{11} \text{ el/m}^3$, while the difference of ICSIRT is about $1 \times 10^{11} \text{ el/m}^3$. The correction of CSIRT is very smooth due to the Laplacian operator smoothing process. However, the ICSIRT correction shows clear horizontal variations since the IDW method can maintain the real corrections.

As shown in Fig. 10, the correction of CSIRT at 00 UT mainly concentrates on the heights from 100 km to 200 km, while ICSIRT concentrates on 300 km and 500 km. At 12 UT, the correction at 300 km of CSIRT is around $3 \times 10^{11} \text{ el/m}^3$. The correction of ICSIRT varies greatly with height,

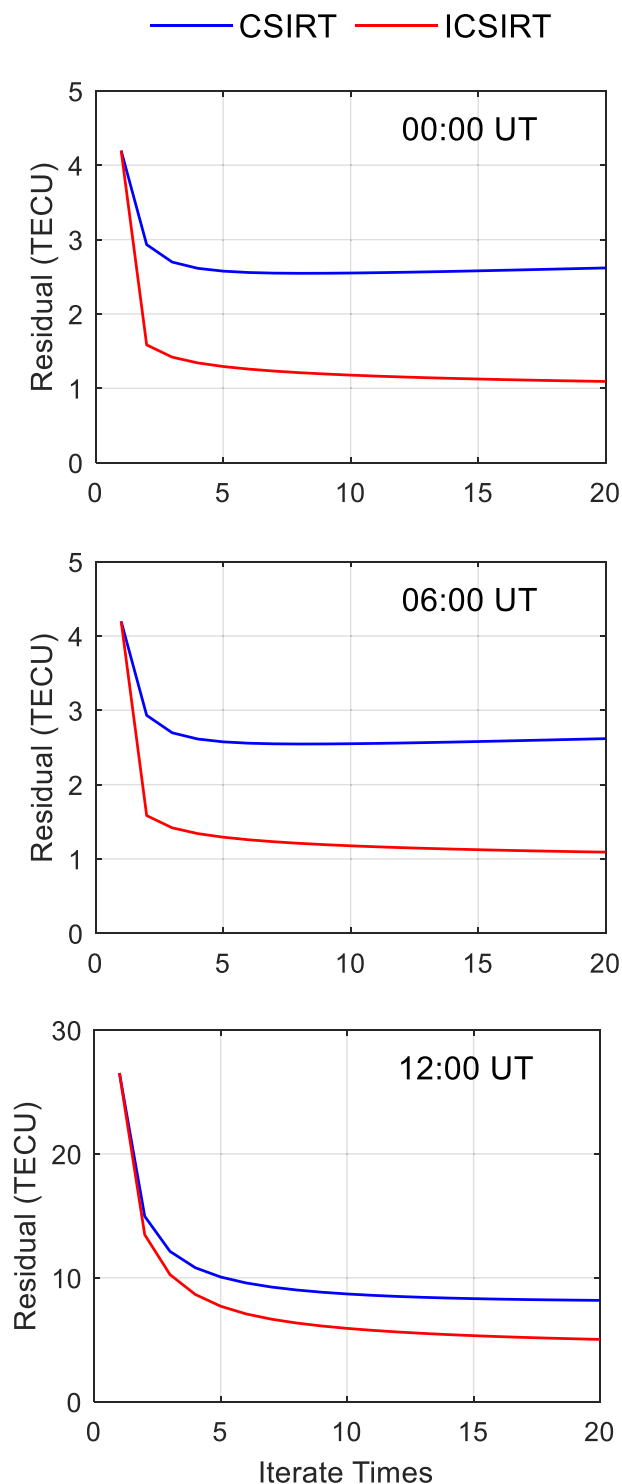
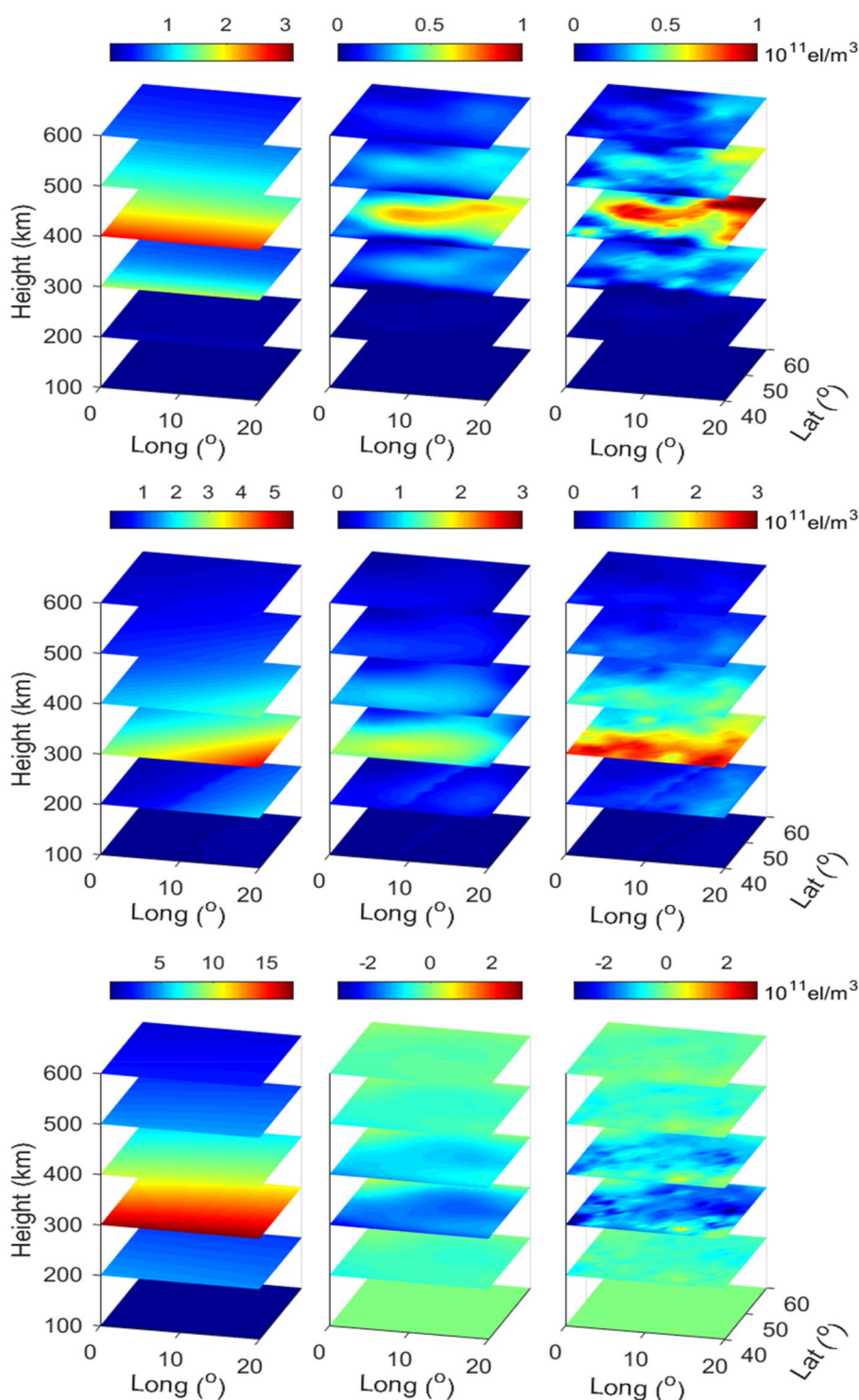


Fig. 8 Comparison of the reconstruction residuals of ICSIRT and CSIRT results. The blue and red curves correspond to the reconstruction residuals of CSIRT and ICSIRT, respectively

and it has the largest correction of $12 \times 10^{11} \text{ el/m}^3$ at 300 km and the smallest correction at the top heights in accordance with the distribution of the electron density at those heights.

Fig. 9 NeQuick2 background and the difference between the reconstruction results and background at 00 UT, 06 UT and 12 UT on March 16, 2013. The first column is the NeQuick2 background, the second column is the difference between the CSIRT reconstruction results and the background, and the third column is the difference between the ICSIRT reconstruction results and the background

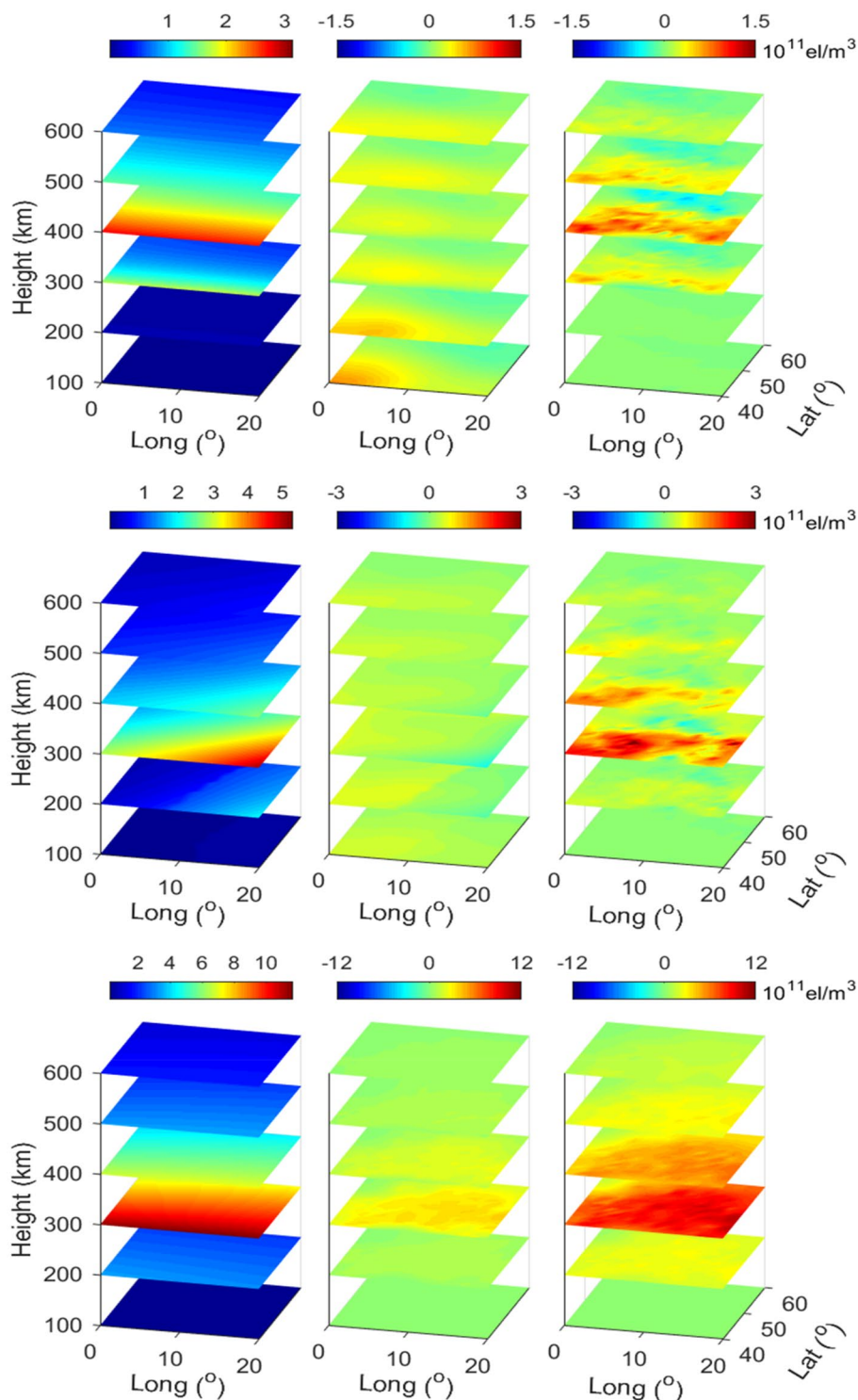


Reconstruction results of June 20 are shown in Fig. 11. At 00 UT, there is a significant density enhancement on the east of inversion region at 300 and 400 km height in ICSIRT results. The enhancement is much smaller in CSIRT results. Electron density enhanced all over the inversion region both

in CSIRT and in ICSIRT at 06 UT. Corrections are larger in ICSIRT results than CSIRT method during June 20.

Figure 12 shows the reconstruction results of September 22. At 00 UT, the inversion region of CSIRT is over-smoothed and does not reflect the differences in the horizontal distribution of the ionosphere since the voxels

Fig. 10 NeQuick2 background and the difference between the reconstruction results and the background at 00 UT, 06 UT and 12 UT on March 17, 2013. The first column is the NeQuick2 background, the second column is the difference between the CSIRT reconstruction results and the background, and the third column is the difference between the ICSIRT reconstruction results and the background

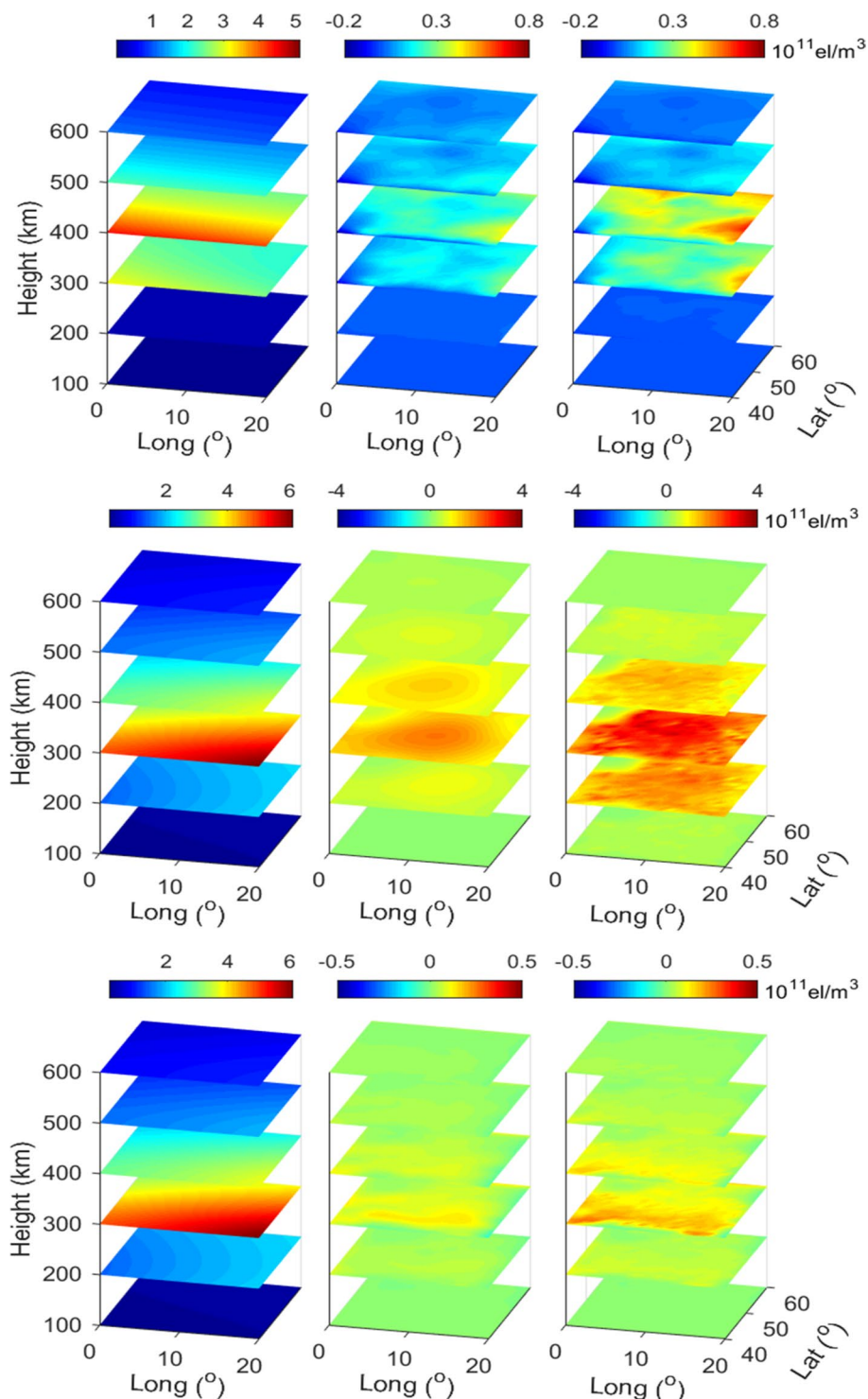


traversed by rays and those not traversed by rays are not discriminated during the smoothing process. In reality, the ionosphere varies drastically in the horizontal distribution due to solar and geomagnetic activities. Since the ICSIRT algorithm uses the IDW interpolation, the inversion region is not over-smoothed. It can be seen at 300 and 400 km that

there are large variations in the horizontal variations in the ICSIRT correction, which better reflects the state of the actual ionosphere.

Figure 13 shows the reconstruction results of December 22. At 12 UT, the CISRT corrections of all heights are negative. However, the ICSIRT differences show positive

Fig. 11 NeQuick2 background and the difference between reconstruction results and the background at 00 UT, 06 UT and 12 UT on June 20, 2013. The first column is the NeQuick2 background, the second column is the difference between the reconstruction results of CSIRT and the background, and the third column is the difference between reconstruction results of ICSIRT and background

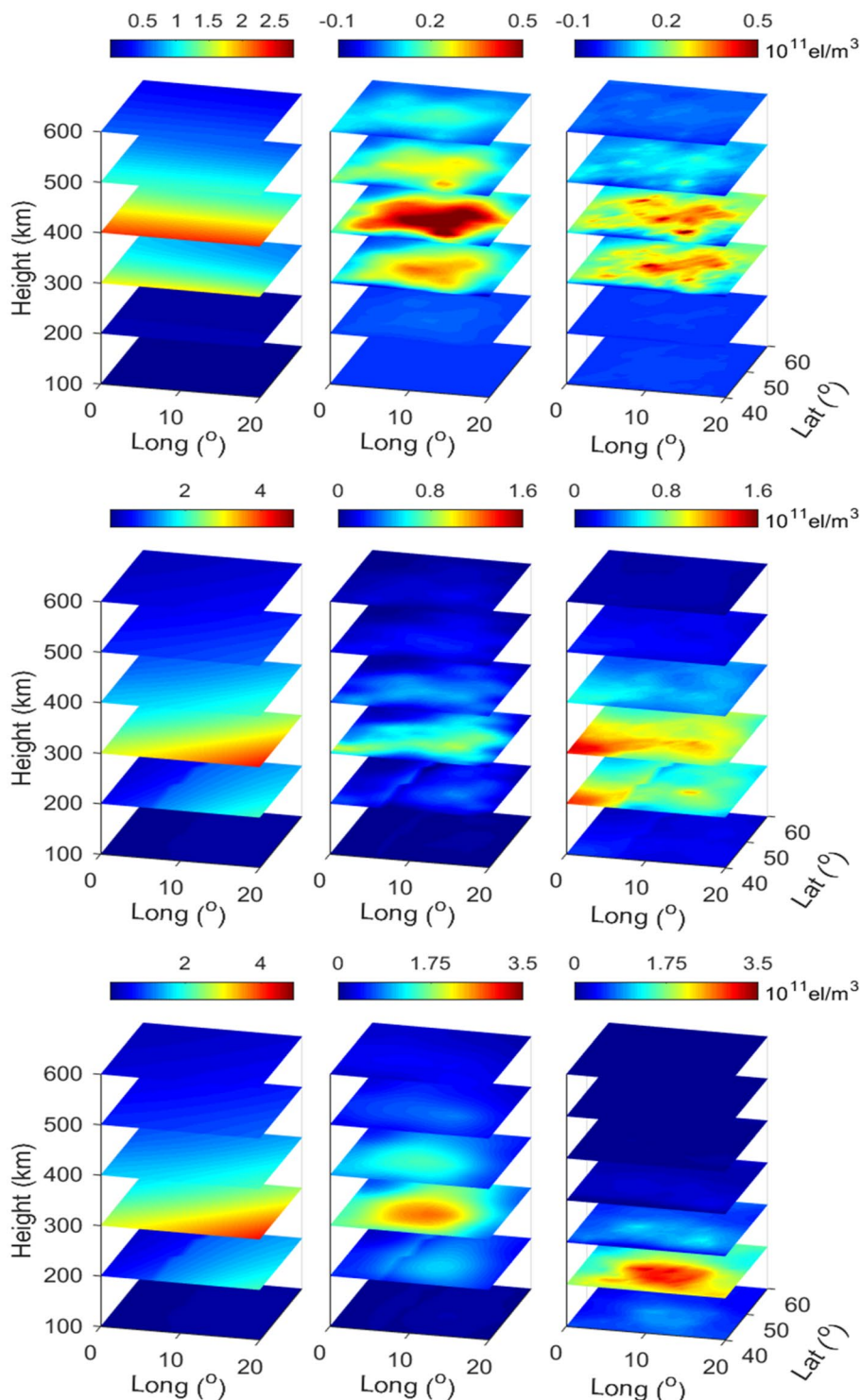


corrections at 200 km and negative corrections from 300 to 600 km, which indicates more variations with heights.

The height plane Figs. 9, 10, 11, 12, 13 can also be analyzed together with Fig. 14, which shows the comparison of the CSIRT and ICSIRT reconstruction results with NeQuick2 and the ionosonde data. It can also be seen from panels (b2), (b3) and (d3) that there are under-corrections

at high electron density heights from 200 to 400 km in the CSIRT results. The NmF2 and profiles below hmF2 of ICSIRT are much closer to the ionosonde observations than NeQuick2 and CSIRT. Since the corrections are based on the product of the intercept and electron density within voxels in the ICSIRT method and IDW interpolation is employed to smooth reconstructed results, the electron density values

Fig. 12 NeQuick2 background and the difference between reconstruction results and the background at 00 UT, 06 UT and 12 UT on September 22, 2013. The first column is the NeQuick2 background, the second column is the difference between the reconstruction results of CSIRT and the background, and the third column is the difference between the reconstruction results of ICSIRT and background

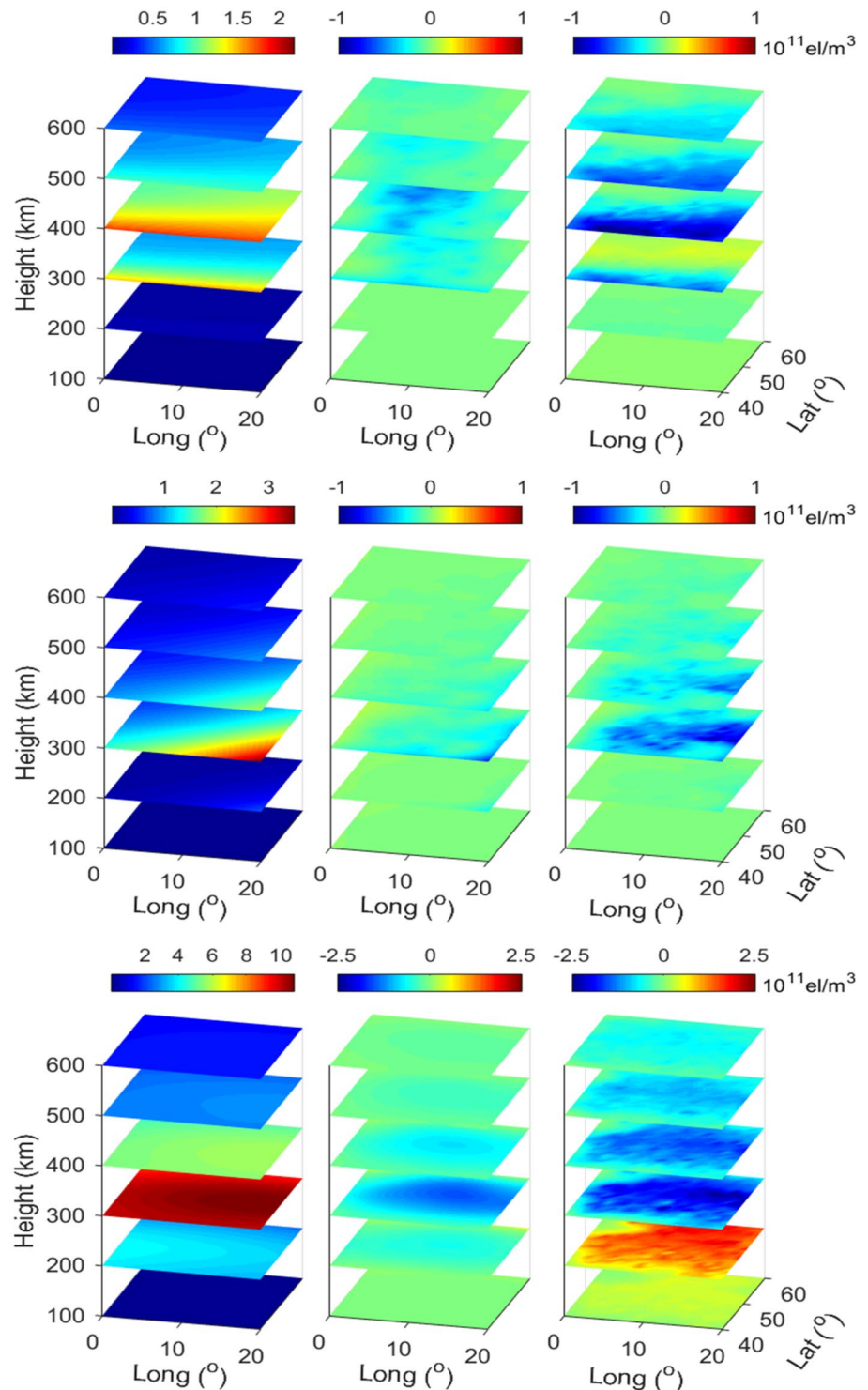


at high density heights are corrected more efficiently and over-smoothing is avoided. As can be seen from Figs. 9, 10, 11, 12, 13, the magnitude of the ICSIRT results is generally larger than that of the CISRT results most of the times.

At 00 UT and 12 UT on March 17, 00 UT on June 20, 00 UT on December 22, Fig. 14 shows that the ICSIRT reconstruction results from 100 km to 300 km almost agree well

with the ionosonde observations. The ICSIRT algorithm has the greatest correction at the peak of electron density, and the NmF2 values of ICSIRT results are much closer to ionosonde observation than CSIRT, especially for 06 UT and 12 UT of March 17, 06 UT of June 20, 12 UT of September 22, and 06 UT of December 22. The ICSIRT density profile is much closer to the ionosonde data for most time.

Fig. 13 NeQuick2 background and the difference between reconstruction results and the background at 00 UT, 06 UT and 12 UT on December 22, 2013. The first column is the NeQuick2 background, the second column is the difference between the reconstruction results of CSIRT and the background, and the third column is the difference between reconstruction results of ICSIRT and background



Since the vertical resolution from 200 km to 420 km is 10 km in ICSIRT and 50 km in CSIRT, the altitude profiles of the ICSIRT results are much smoother than those of CSIRT and also closer to the ionosonde observations. It should be noted that the topside ionosonde profiles are extrapolated from bottom side data based on certain

assumptions (Reinisch et al. 2001) and, therefore, uncertainty in these topside ionosonde data is expected.

To assess the accuracy of the reconstructed electron density profiles, we have taken the ionosonde measurements from 100 km to the altitude of HmF2 as true values, and calculated the Root Mean Square error (RMSE) of the CSIRT

Fig. 14 Comparison of electron density profiles at 00 UT, 06 UT and 12 UT on March 16, March 17, June 20, September 22, December 22, 2013. The red curve is the ionosonde data, the black dashed line is NeQuick2 background, the blue solid dotted curve is the CSIRT reconstruction result, and the green solid dotted line is the ICSIRT reconstruction result

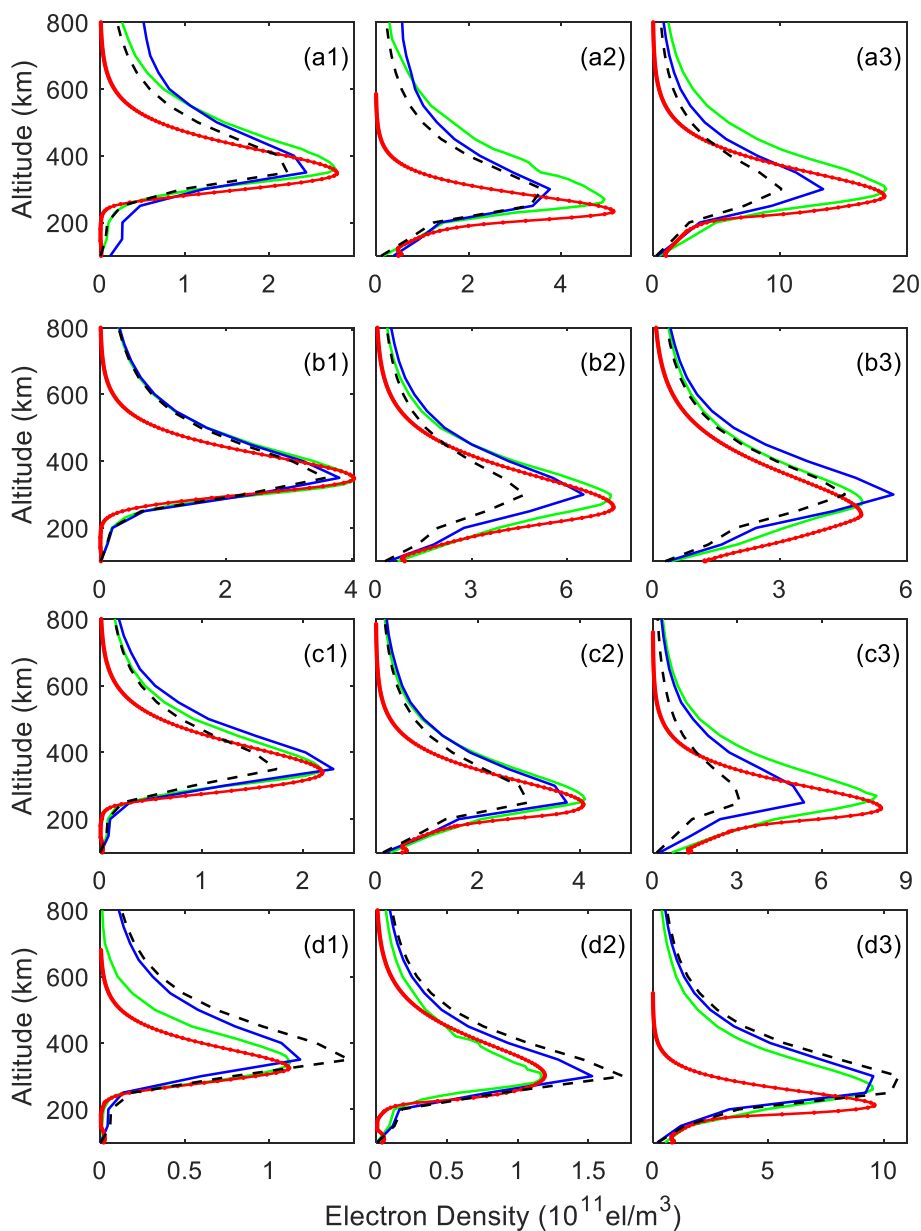
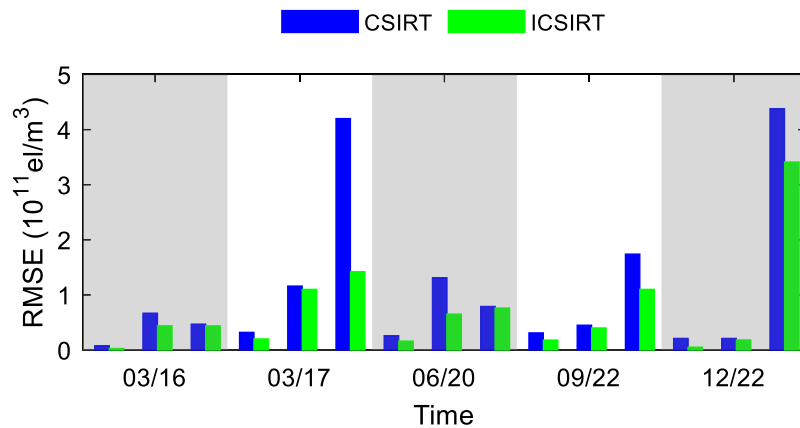


Fig. 15 Comparison of RMSE of electron density profile from 100 km to HmF2 between CSIRT and ICSIRT results. The blue and green bars represent the RMSE of CSIRT and ICSIRT, respectively. Data for different days are differentiated with shadows. The time of three bars from left to right in every zone is 00 UT, 06 UT and 12 UT



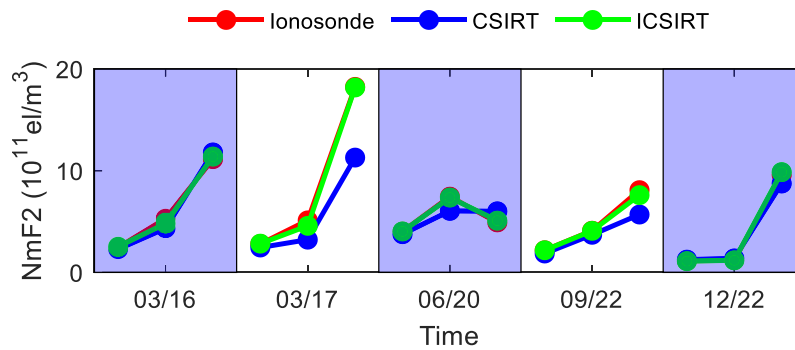


Fig. 16 Comparison of NmF2 derived from the ionosonde measurements, and the CSIRT and ICSIRT reconstruction results. The blue and green dotted lines represent the NmF2 values from CSIRT and

ICSIRT, respectively. Data for different days are differentiated with shadows. The time of three dots from left to right in every zone is 00 UT, 06 UT and 12 UT

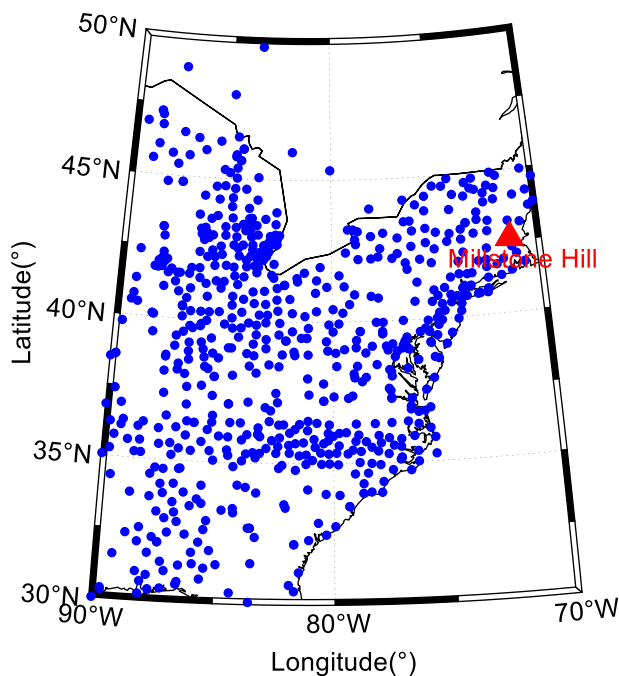


Fig. 17 North American inversion area and distribution of GNSS stations and the Millstone Hill incoherent scatter radar station. The blue dots represent the GNSS stations, and the red triangle represents the ISR station at Millstone Hill

and ICSIRT profiles. The results are shown in Fig. 15. The blue and green bars represent the RMSE of the CSIRT and ICSIRT profiles, respectively. It can be seen from the figure that the accuracy of ICSIRT is better than CSIRT for all time periods, especially at March 17 at 12 UT: the RMSE of CSIRT is 4.20×10^{11} el/m³ while the RMSE of ICSIRT is 1.42×10^{11} el/m³.

Figure 16 shows the NmF2 comparisons between the ionosonde measurements (red dotted line) and the CSIRT (blue dotted line) and ICSIRT reconstruction results (green dotted line). The NmF2 values retrieved from the ICSIRT

Table 1 Experiment time of North American region

Time (UT)	Subfigure
03/17	00:00 (a1)
	06:00 (a2)
	18:00 (a3)
06/20	13:44 (b1)
	16:06 (b2)
	19:30 (b3)
09/26	12:33 (c1)
	15:56 (c2)
	19:11 (c3)
12/17	12:28 (d1)
	17:01 (d2)
	23:38 (d3)

results are much closer to the ionosonde measurements than the CSIRT results, especially at 12 UT on March 17 and 12 UT on September 22.

Real data experiment: North American region

For further evaluation of ICSIRT electron density profiles, the ionospheric electron density over the North American region is reconstructed and compared to Millstone Hill incoherent scatter radar (ISR) as the radar can show the entire electron density profile from about 100 km to about 800 km. The inversion region is 30°–50°N in latitude and 70°–90°W in longitude, and the height ranged from 100 to 800 km. The geographic distribution of the GNSS and ISR stations is given in Fig. 17, and the experiment times are given in Table 1. The experiment times are chosen according to the ISR data availability.

Figure 18 shows the comparison of electron density profiles between 3DCIT results and ISR observations. The

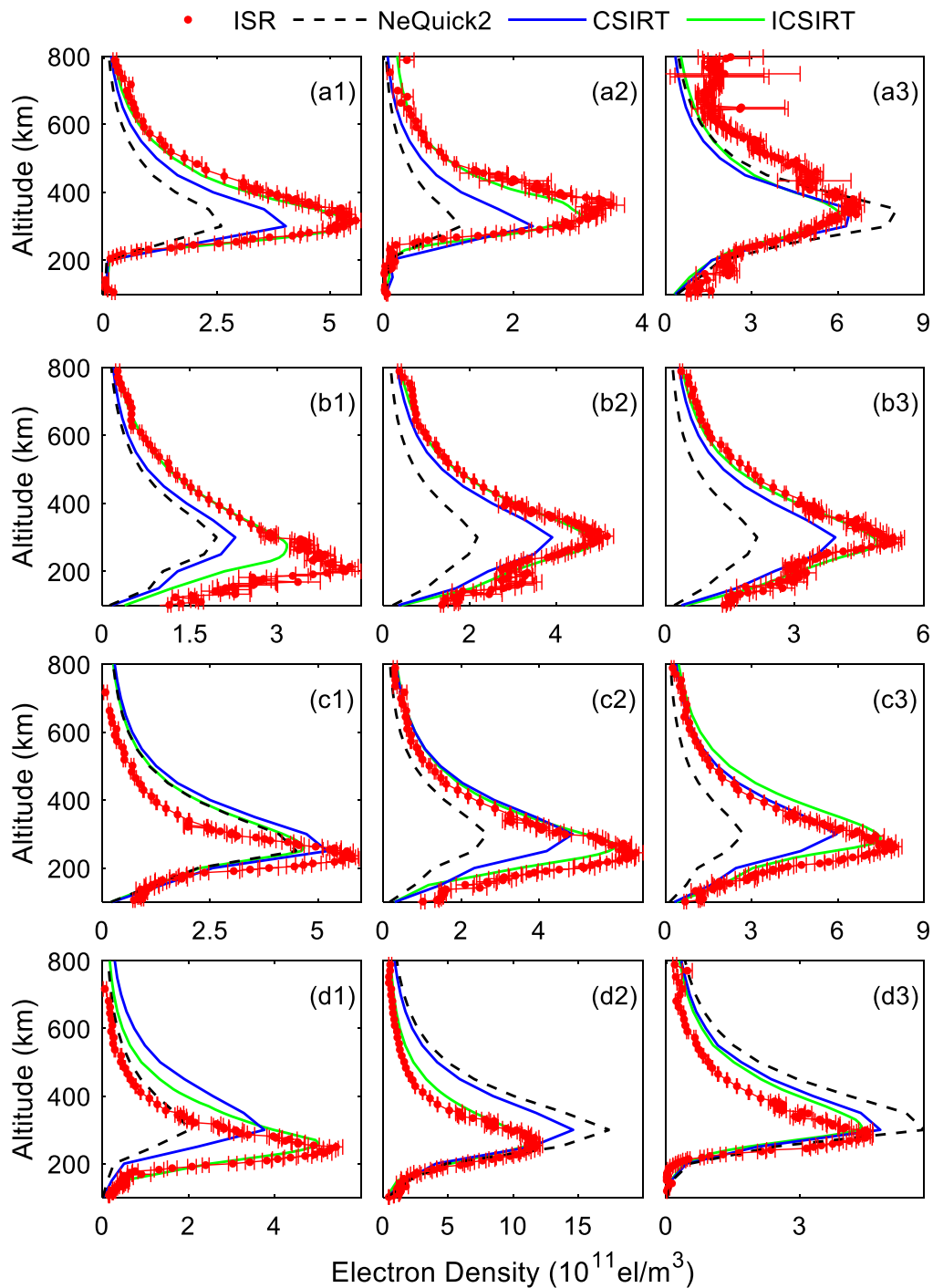


Fig. 18 Comparison of electron density profiles between reconstruction results and ISR. The panels from top to bottom are March 17, June 20, September 26, December 17, 2013. The red dots are ISR

data, the black dashed line is NeQuick2 background, the blue solid dotted curve is the CSIRT reconstruction result, and the green solid dotted line is the ICSIRT reconstruction result

panels from top to bottom are March 17, June 20, September 26, December 17, 2013. The red dots are ISR data, the black dashed line is NeQuick2 background, the blue solid dotted curve is the CSIRT reconstruction result, and the green solid dotted line is the ICSIRT reconstruction

result. The ICSIRT results obtained more correction, and the entire profiles are closer to ISR profiles in most of the times. The ICSIRT results show a good agreement with ISR profiles in panels (a1), (a2), (b2) and (d2), especially for the topside profiles. Benefitting from a higher vertical

resolution around F2 peak altitude, the HmF2 of ICSIRT results also performed better than CSIRT results in panels (c2), (d1) and (d2).

Conclusions and discussions

An improved CSIRT reconstruction algorithm is presented in this research. The new algorithm optimizes the correction allocation method by using the product of electron density and intercept instead of the traditional method that uses the intercepts of ray paths within voxels. Therefore, the receive correction of the voxels is proportional to their respective electron densities. Inverse distance weighted interpolation is also applied to correct the voxels not traversed by the GNSS rays to ensure the smoothness of the reconstruction results. Finally, the method makes more effective use of the GNSS observation data, and the reconstruction area is much improved.

Case studies have been conducted in the European region and the North American region under different seasons and solar activities. In the European region experiment, the ICSIRT algorithm significantly reduces the residuals of the reconstructed results and produces more realistic reconstruction results. The ICSIRT results obtained larger magnitudes of corrections than CSIRT results around electron density peak heights most of the times. Furthermore, there are more detailed horizontal variations of electron density in the ICSIRT results, such as at 00 UT on both June 20 and September 22. Since a multiresolution is employed in the ICSIRT method, the profiles of ICSIRT results perform much smoother and closer to ionosonde profiles from 200 to 400 km. The RMSE of ICSIRT electron density profiles from 100 km to HmF2 is improved by 66.2% compared to the CSIRT results and NmF2 values of ICSIRT coincide with ionosonde values.

In the North American region experiment, the reconstruction results of two approaches are compared to ISR observations since the radar data can determine the whole electron density profile. The ICSIRT profiles show better consistency with ISR profiles even for topside profiles such as panels (a1) and (b1) in Fig. 18. Since a multi-vertical resolution is employed, the ICSIRT method can reconstruct the electron density vertical distribution more precisely around F2 peak height. In panels (c2), (d1) and (d2) of Fig. 18, the HmF2 values of ICSIRT results are much closer to ISR data than CSIRT. The experiment in the North American region further demonstrates the superiority of ICSIRT to traditional approaches.

Acknowledgements The authors would like to thank EUREF Permanent GNSS Network (EPN) for providing the Global Navigation Satellite System (GNSS) data and Global Ionospheric Radio Observatory

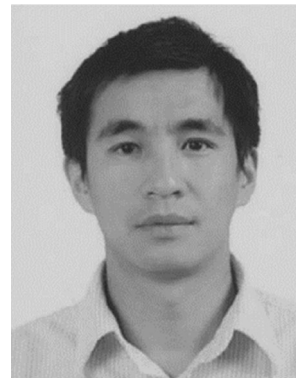
(GIRO) for providing the ionosonde data. We acknowledge Telecommunications/ICT for Development (T/ICT4D) Laboratory of the Abdus Salam International Centre for Theoretical Physics, Trieste, Italy, for providing NeQuick2 model. The GNSS data are obtained from <ftp://epncb.oma.be/>, and the ionosonde data are obtained from <ftp://ngdc.noaa.gov/ionosonde/data/>. We also thank MIT Haystack Observatory for providing incoherent scatter radar data. Millstone Hill ISR data can be download from <http://cedar.openmadrigal.org>. Radar observations and analysis at Millstone Hill and the Madrigal distributed database system are supported by the US National Science Foundation Cooperative Agreement AGS-1762141 with the Massachusetts Institute of Technology. This research was supported by (1) National Natural Science Foundation Innovation Research Group Project (Grant NO. 41721003); (2) National Natural Fund of China (41604002) Open Research Fund of State Key; (3) Laboratory of Information Engineering in Surveying, Mapping and Remote Sensing, Wuhan University (18P02); (4) Key Laboratory of Geospace Environment and Geodesy, Ministry of Education, Wuhan University (170208)

References

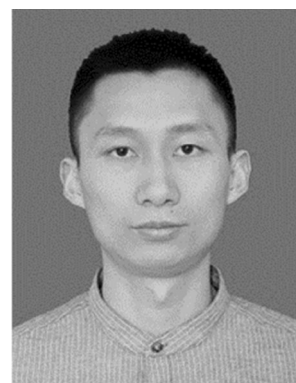
- Andreeva ES, Galinov AV, Kunitsyn VE, Melnichenko YA, Tereshchenko ED, Filimonov MA, Chernyakov SM (1990) Radiotomographic reconstruction of ionization dip in the plasma near the Earth. *JETP Lett* 52(3):145–148
- Austen JR, Franke SJ, Liu CH (1988) Ionospheric imaging using computerized tomography. *Radio Sci* 23(3):299–307
- Bruyninx C, Legrand J, Fabian A, Pottiaux E (2019) GNSS metadata and data validation in the EUREF permanent network. *GPS Solut* 23:106. <https://doi.org/10.1007/s10291-019-0880-9>
- Bust GS, Mitchell CN (2008) History, current state, and future directions of ionospheric imaging. *Rev Geophys* 46(RG1003):1–23
- Chasovitin YK (1998) Russian standard model of ionosphere (SMI). In: *Proceedings of COST251*, pp 161–172
- Cherniak I, Zakharenkova I (2016) NeQuick and IRI-Plas model performance on topside electron content representation: spaceborne GPS measurements. *Radio Sci* 51(6):752–766
- Debao W, Xiao Z, Yangjin T, Guangsheng Z, Min Z, Rusong L (2015) GPS-based ionospheric tomography with a constrained adaptive simultaneous algebraic reconstruction technique. *J Earth Syst Sci* 124(2):283–289
- ElArini MB, Conker RS, Albertson TW, Reagan JK, Klobuchar JA, Doherty PH (1994) Comparison of real-time ionospheric algorithms for a GPS wide-area augmentation system (WAAS). *Navigation* 41(4):393–414
- Galkin IA, Reinisch BW, Huang X, Bilitza D (2012) Assimilation of GIRO data into a real-time IRI. *Radio Sci*. <https://doi.org/10.1029/2011rs004952>
- Ge L, Chang HC, Janssen V, Rizos C (2003) Integration of GPS, radar interferometry and GIS for ground deformation monitoring. In: *Proceedings of 2003 international symposium on GPS/GNSS*, Tokyo, Japan, pp 465–472
- Gordon R, Bender R, Herman GT (1970) Algebraic reconstruction techniques (ART) for three-dimensional electron microscopy and X-ray photography. *J Theor Biol* 29(3):471–477
- Gulyaeva TL (2002) The ionosphere-plasmasphere model software for ISO. *Acta Geod Geophys Hungar* 37(3):143–152
- Hobiger T, Kondo T, Koyama Y (2008) Constrained simultaneous algebraic reconstruction technique (C-SART)—a new and simple algorithm applied to ionospheric tomography. *Earth Planets Space* 60(7):727–735

- Huang CR, Liu CH, Yeh KC, Lin KH, Tsai WH, Yeh HC, Liu JY (1999) A study of tomographically reconstructed ionospheric images during a solar eclipse. *J Geophys Res Space Phys* 104(A1):79–94
- Jin R, Jin S, Feng G (2012) M_DCB: matlab code for estimating GNSS satellite and receiver differential code biases. *GPS Solut* 16(4):541–548. <https://doi.org/10.1007/s10291-012-0279-3>
- Kersley L, Heaton JAT, Pryse SE, Raymund TD (1993) Experimental ionospheric tomography with ionosonde input and EISCAT verification. *Ann Geophys Germany* 11:1064–1074
- Kong J, Yao Y, Liu L, Zhai C, Wang Z (2016) A new computerized ionosphere tomography model using the mapping function and an application to the study of seismic-ionosphere disturbance. *J Geodesy* 90(8):741–755
- Kunitsyn VE, Andreeva ES, Razinkov OG, Tereshchenko ED (1994a) Phase and phase-difference ionospheric radio tomography. *Int J Image Syst Technol* 5(2):128–140
- Kunitsyn VE, Andreeva ES, Tereshchenko ED, Khudukon BZ, Nygren T (1994b) Investigations of the ionosphere by satellite radiotomography. *Int J Image Syst Technol* 5(2):112–127
- Kunitsyn VE, Andreeva ES, Popov AY, Razinkov OG (1995) Methods and algorithms of ray radiotomography for ionospheric research. *Ann Geophys* 13(12):1263–1276
- Kunitsyn VE, Andreeva ES, Razinkov OG (1997) Possibilities of the near-space environment radio tomography. *Radio Sci* 32(5):1953–1963
- Liu S, Wang J, Gao J (2010) Inversion of ionospheric electron density based on a constrained simultaneous iteration reconstruction technique. *IEEE TGRS* 48(6):2455–2459
- Markkanen M, Lehtinen M, Nygrén T, Pirttilä J, Henelius P, Vilenius E, Tereshchenko ED, Khudukon BZ (1995) Bayesian approach to satellite radiotomography with applications in the Scandinavian sector. *ISME J* 8(11):2280–2289
- Nava B, Coisson P, Radicella SM (2008) A new version of the NeQuick ionosphere electron density model. *J Atmos Sol Terr Phy* 70(15):1856–1862
- Norberg J, Roininen L, Vierinen J, Amm O, McKay-Bukowski D, Lehtinen M (2015) Ionospheric tomography in Bayesian framework with Gaussian Markov random field priors. *Radio Sci* 50(2):138–152
- Prasad N, Sarma AD (2007) Preliminary analysis of grid ionospheric vertical error for GAGAN. *GPS Solut* 11(4):281–288
- Pryse SE, Kersley L, Rice DL, Russell CD, Walker IK (1993) Tomographic imaging of the ionospheric mid-latitude trough. *Ann Geophys* 11(2):144–149
- Pryse SE, Kersley L, Williams MJ, Walker IK, Willson CA (1997) Tomographic imaging of the polar-cap ionosphere over Svalbard. *J Atmos Sol Terr Phy* 59(15):1953–1959
- Raymond TD, Franke SJ, Yeh KC (1994) Ionospheric tomography: its limitations and reconstruction methods. *J Atmos Terr Phys* 56(5):637–653
- Raymund TD, Austen JR, Franke SJ, Liu CH, Klobuchar JA, Stalker J (1990) Application of computerized tomography to the investigation of ionospheric structures. *Radio Sci* 25(05):771–789
- Reinisch BW, Galkin IA (2011) Global ionospheric radio observatory (GIRO). *Earth Planets Space* 63(4):377–381. <https://doi.org/10.5047/eps.2011.03.001>
- Reinisch BW, Huang X (2001) Deducing topside profiles and total electron content from bottomside ionograms. *Adv Space Res* 27(1):23–30. [https://doi.org/10.1016/S0273-1177\(00\)00136-8](https://doi.org/10.1016/S0273-1177(00)00136-8)
- Shim JS, Jee G, Scherliess L (2017) Climatology of plasmaspheric total electron content obtained from Jason 1 satellite. *J Geophys Res Space Phys* 122(2):1611–1623
- Wan X, Zhang F, Chu Q, Zhang K, Sun F, Yuan B, Liu Z (2011) Three-dimensional reconstruction using an adaptive simultaneous algebraic reconstruction technique in electron tomography. *J Struct Biol* 175(3):277–287
- Wen D, Yuan Y, Ou J, Huo X, Zhang K (2007) Three-dimensional ionospheric tomography by an improved algebraic reconstruction technique. *GPS Solut* 11(4):251–258
- Wen D, Yuan Y, Ou J, Zhang K, Liu K (2008) A hybrid reconstruction algorithm for 3-D ionospheric tomography. *IEEE Trans Geosci Remote* 46(6):1733–1739. <https://doi.org/10.1109/TGRS.2008.916466>
- Wen D, Liu S, Tang P (2010) Tomographic reconstruction of ionospheric electron density based on constrained algebraic reconstruction technique. *GPS Solut* 14(4):375–380. <https://doi.org/10.1007/s10291-010-0161-0>
- Wen D, Wang Y, Norman R (2012) A new two-step algorithm for ionospheric tomography solution. *GPS Solut* 16(1):89–94. <https://doi.org/10.1007/s10291-011-0211-2>
- Yao Y, Tang J, Chen P, Zhang S, Chen J (2014) An improved iterative algorithm for 3-D ionospheric tomography reconstruction. *IEEE Trans Geosci Remote* 52(8):4696–4706
- Yao Y, Zhai C, Kong J, Zhao Q, Zhao C (2018) A modified three-dimensional ionospheric tomography algorithm with side rays. *GPS Solut* 22(4):107
- Zhang M, Liu L, Wan W, Ning B (2017) Comparison of the observed topside ionospheric and plasmaspheric electron content derived from the COSMIC podTEC measurements with the IRI_Plus model results. *Adv Space Res* 60(2):222–227

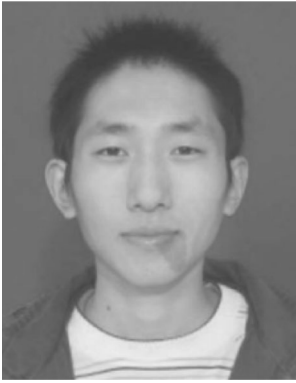
Publisher's Note Springer Nature remains neutral with regard to jurisdictional claims in published maps and institutional affiliations.



Yibin Yao is currently a Professor at the School of Geodesy and Geomatics, Wuhan University. He received the Ph.D. degree from Wuhan University, Wuhan, China, 2004. He is also with the Collaborative Innovation Center for Geospatial Technology, Wuhan. His main research interests include GNSS, ionospheric atmospheric meteorological studies, theory, and method of surveying data processing.



Changzhi Zhai is currently working toward the Ph.D. degree in geodesy and surveying engineering in the School of Geodesy and Geomatics, Wuhan University, Wuhan, China. He received an M.Sc. degree from Wuhan University, Wuhan, China, in 2017. His research interests include Global Navigation Satellite System (GNSS) data processing and 3-D ionospheric tomography based on GNSS observations.



Jian Kong received a B.Sc. degree from Shandong University of Science and Technology, Qingdao, China, in 2009 and a Ph.D. degree from Wuhan University, Wuhan, China, in 2014. His main research interests include GNSS data processing, global ionospheric modeling using multisource geodesy observations, 3-D ionospheric tomography based on GNSS observations, and ionospheric anomalies analysis under abnormal conditions.



Yiyong Luo received the B.Eng. Degree from East China University of Technology, Nanchang, China, in 2006 and the M.Sc. degree from East China University of Technology, Nanchang, China, in 2009. He is currently working toward the Ph.D. degree in geodesy and surveying engineering in the School of Geodesy and Geomatics, Wuhan University, Wuhan, China. His research interests include Global Navigation Satellite System (GNSS) data processing and 3-D ionospheric tomography based

on GNSS observations.



Cunjie Zhao is currently working toward the Ph.D. degree in geodesy and surveying engineering in the School of Geodesy and Geomatics, Wuhan University, Wuhan, China. He received an M.Sc. degree from Wuhan University, Wuhan, China, in 2015. His research interests include Global Navigation Satellite System (GNSS) data processing and 3-D ionospheric tomography based on GNSS observations.



Lei Liu received the B.Sc. degree from Central South University of Forestry and Technology, Changsha China, in 2014 and the M.Sc. degree from Wuhan University, Wuhan, China, in 2017. He is currently working toward the Ph.D. degree in geodesy and surveying engineering in the School of Geodesy and Geomatics, Wuhan University, Wuhan, China. His research interests include Global Navigation Satellite System (GNSS) data processing and 3-D ionospheric tomography based on GNSS

observations.